Spatially resolved two-dimensional Fourier transform electron spin resonance

Uwe Ewert [1], Richard H. Crepeau, Sanghyuk Lee, Curt R. Dunnam [2], Dajiang Xu and Jack H. Freed

Baker Laboratory of Chemistry, Cornell University, Ithaca, NY 14853, USA

Received 17 May 1991; in final form 2 July 1991

Fourier transform ESR methods have been extended to permit spatially resolved two-dimensional (2D)-ESR experiments. This is illustrated for the case of 2D-electron–electron double resonance (2D-ELDOR) spectra of nitroxides in a liquid that exhibits appreciable cross-peaks due to Heisenberg spin exchange. The use of spin-echo decays in spatially resolved FT-ESR is also demonstrated.

1. Introduction

In the accompaning Letter [1] we have described successful FT-ESR imaging experiments utilizing pulsed field gradients. It was shown that the phase encoding method is the preferred one, and it yields spectral–spatial images of a quality comparable to the best cw-ESR spectral–spatial images even though it is only at an early stage of development.

The realization of these FT-ESR imaging experiments opens up a range of new possibilities. One is the possibility of performing spatially resolved ESR spectroscopies based upon modern FT methods. In particular, we shall emphasize in this Letter spatially resolved two-dimensional electron–electron double resonance (2D-ELDOR) [2–7]. 2D-ELDOR is a form of 2D-exchange spectroscopy that is very sensitive to cross-relaxation processes including Heisenberg spin exchange (HE) and nuclear spin flips induced by electron–nuclear dipolar interactions. They are important measures of microscopic translational diffusion, and rotational diffusion respectively. Spatial resolution would, for example, permit one to study microscopic molecular dynamics in inhomogeneous media.

Another potential application of 2D-ELDOR would be the ability to study simultaneously, on the same sample, both macroscopic and microscopic translational diffusion. Recently this was demonstrated by cw spectral–spatial imaging of a sample with an inhomogeneous concentration distribution [8]. One may image macroscopic diffusion by observing, in the spatial dimension as a function of time, how the concentration distribution spreads. The ESR linewidths may be measured in the spectral dimension, and from the observed concentration variation of these widths, the HE and intermolecular electron–electron spin dipolar (EED) contributions may be estimated to yield microscopic relative diffusion coefficients. The microscopic and macroscopic diffusion coefficients are found to be different in complex fluids, and such combined studies may be expected to provide better insight into microscopic molecular dynamics.

However, cw-ESR linewidths are not the best way to study microscopic translational diffusion [3,9]. One must extract the concentration-dependent widths from other sources of homogeneous and inhomogeneous broadening. Furthermore, the separation of these concentration-dependent widths into HE and EED components is, in general, not straightforward

[1] Currently at Centre of Scientific Instruments of the Academy of Sciences of the DDR, Berlin.

[2] Laboratory of Nuclear Studies, Cornell University, Ithaca, NY.

and subject to uncertainties. 2D-ELDOR has been shown to be a natural way to directly measure HE from the cross-peaks [4]. (Included in this point is the fact that EED is significantly suppressed in the ELDOR versus the linewidths.) Thus spatially resolved ELDOR could be the method of choice for comparative studies of microscopic versus macroscopic diffusion.

Additionally, one could employ other 1D or 2D pulsed ESR techniques [5,6] along with spatial resolution. For example, by performing spatially resolved spin echoes one could obtain just the *homogeneous* contributions to the linewidths (i.e. the inverse T_2's), which represents a significant improvement over cw-ESR linewidths for studies of molecular dynamics. This would be a spatially resolved SECSY (spin-echo correlation spectroscopy) experiment [5,6]. Thus, while we have primarily focused on FT-ESR imaging based upon FIDs, it is important to consider FT-ESR imaging based upon spin echo decays. More generally, this technique would permit FT-ESR imaging in cases where the inhomogeneous broadening (i.e. inverse T_2^*) is too great, in comparison to the deadtime of the experiment, to allow the observation of the FID, a situation that is true for many powder samples or samples exhibiting slow-motional spectra. It is also true for imaging with large field gradients in the frequency encoding mode. Despite the shortness of the echo decay typical of such samples, recent developments in 2D-FT-ESR techniques now permit such experiments [10–12]. Echo decays will accurately mirror the FIDs in cases where the T_2 relaxation is uniform over the spectrum and nuclear modulation effects are unimportant [10,11].

In this Letter we demonstrate, with a test sample of liquids, spatially resolved 2D-ELDOR with appreciable HE-induced cross-peaks imaged by FID detection using the fast gradient pulses described earlier [1]. We also demonstrate, with a solid-state sample, spatial–spatial and spectral–spatial imaging in the presence of a stationary gradient based upon collection of the full echo decay shape.

2. Theoretical expressions

The pulse sequence for the 2D-ELDOR experiment is shown in fig. 3. Its theoretical description is a generalization of the single pulse experiments described in ref. [1]. Here we just consider phase encoding the magnetization with a gradient pulse, G, which can be varied from $-G_{\max}$ to $G_{\max}$. Let $S'_{0,\mathrm{ELDOR}}(T, t_1, t_2, c(x))$ be the complex ELDOR signal at time t_2 after the third $\pi/2$ pulse with no field gradient applied. (There is also a second complex signal $S''_{0,\mathrm{ELDOR}}(T, t_1, t_2, c(x))$ required for the *dual* quadrature detection and obtained by repeating the experiment with a phase shift of the first pulse [2,4–6].) The signal potentially depends on the spin concentration, $c(x)$. If a field gradient G is applied for a period τ ($\tau<t_1$), just after the first $\pi/2$ pulse, we have the observed signal during t_2:

$$\bar{S}'_{\mathrm{p,ELDOR}}(T, t_1, t_2, G) = \int_{-\infty}^{\infty} c(x) \exp(-ikx) \times S'_{0,\mathrm{ELDOR}}(T, t_1, t_2, x)\, \mathrm{d}x\,, \tag{1}$$

where $k=\gamma_e G\tau$. The Fourier inverse of eq. (1) is

$$c(x)S'_{0,\mathrm{ELDOR}}(T, t_1, t_2, x) = (1/2\pi) \times \int_{-\infty}^{\infty} \exp(ikx)\, \bar{S}'_{\mathrm{p,ELDOR}}(T, t_1, t_2, k/\gamma_e\tau)\, \mathrm{d}k\,. \tag{2}$$

If we now perform the double FT in t_1, and t_2, we obtain: $c,(x)\tilde{S}'_{0,\mathrm{ELDOR}}(T, \omega_1, \omega_2, x)$.

The form of $S'_{0,\mathrm{ELDOR}}$ may be obtained from recent treatments [4–6]. In our experiments with nitroxides at substantial concentrations, the HE mechanism is the dominant mechanism generating the cross-peaks. In this case $S'_{0,\mathrm{ELDOR}}$ can be written as a sum of auto-peaks (2 for ^{15}N and 2 for ^{14}N) and of cross-peaks (2 for ^{15}N and 6 for ^{14}N). The j, mth peak is described by

$$\tilde{S}'_{\mathrm{ELDOR}}(T, \omega_1, \omega_2, j, m) = B\left(\frac{\mathrm{i}(\omega_j-\omega_1)+T_{2,j}}{(\omega_1-\omega_j)^2T_{2,j}^2+1}\right) \times \bar{Q}_{j,m}(T)\left(\frac{T_{2,m}}{(\omega_2-\omega_m)^2T_{2,m}^2+1}\right), \tag{3}$$

where for an auto-peak, $j=m$,

$$\bar{Q}_{m,m}(T) = \exp(-2W_eT) + 2\exp[-(2W_e+\omega_{\mathrm{HE}})T] \tag{4}$$

and for cross-peaks, $j \neq m$,

$$\bar{Q}_{j,m}(T) = \exp(-2W_e T) - \exp[-(2W_e + \omega_{HE})T] . \quad (5)$$

Here W_e and ω_{HE} are the electron-spin relaxation rate and HE rate respectively, ω_j and $T_{2,j}$ are the resonant frequency and T_2 of the jth hyperfine line, and B is a spectrometer constant.

The pulse sequence for spin echo (or SECSY) imaging is $\pi/2$–t_1–$\pi/2$–t_1–t_2 with the gradient applied after the first pulse during t_1 and the echo collected during t_2. In this phase encoding experiment, eqs. (1) and (2) may be utilized but with $S'_{0,ELDOR}$ and $\bar{S}'_{p,ELDOR}$ replaced by $S'_{0,SECSY}(t_1, t_2, x)$ and $\bar{S}'_{p,SECSY}(t_1, t_2, G)$, respectively. Spatially resolved SECSY-ESR would be obtained in an analogous fashion to that for ELDOR as outlined above.

In the frequency encoding experiment, we have for the spin echo (SE) by analogy to eq. (5) of ref. [1]

$$\bar{S}'_{SE,f}(t_1, t_2, G) = \int_{-\infty}^{\infty} c(x) \exp(-ikx)\, S'_{SE,0}(t_1, t_2, x)\, dx , \quad (6)$$

where $k = \gamma_e G t_2$ in the case of a constant gradient, cf. fig. 4d (and $k = -\gamma_e G t_1$ if we let the gradient be on for just the period between the two $\pi/2$ pulses). Eq. (6) can be FTd to obtain $c(x)S'_{SE,0}(t_1, t_2, x)$. In the case of an inhomogeneously broadened line composed of many simple spin packets (each labelled by j) we write

$$S'_{SE,0}(t_1, t_2, x) = \sum_j a_j \exp[-(i\omega_j + T_{2,j})t_2] \times \exp(-T_{2,j} t_1) , \quad (7)$$

which illustrates that the inhomogeneous broadening is removed along the t_1 axis. Then if eq. (7) is inserted into eq. (6), we see that for the pulsed gradient with $k = -\gamma_e G t_1$ one can improve resolution due to the elimination of inhomogeneous broadening [13,14]. In a standard SE experiment one optimizes spatial resolution by setting $t_2 = 0$ (cf. fig. 4d). (Appropriate generalizations of eq. (7) may be written for slow-motional ESR spectra [5,6].) If $S'_{SE,0}(t_1, t_2)$ is independent of x we have

$$\bar{S}'_{SE,f}(t_1, t_2, G) = S'_{SE,0}(t_1, t_2)\tilde{c}(k) . \quad (8)$$

Spectra–spatial imaging by frequency encoding (cf. eq. (6)) may be obtained by fixing t_1, letting $k = \gamma_e G t_2$, and collecting the echo decay. It is analogous to using the FID and eq. (5) of ref. [1] except that one selects $t_1 > \tau_d$ to overcome deadtime problems. Multiple stepped gradients are again utilized and back-projection methods are required.

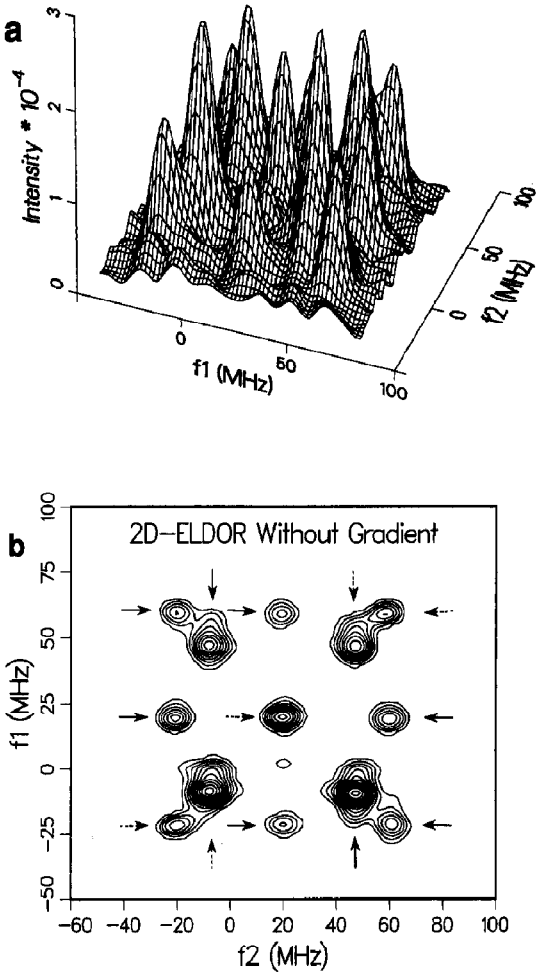

Fig. 1. (a) Surface plot of 2D-ELDOR of sample used in ref. [1] (cf. fig. 1a of ref. [1]) taken in the absence of a field gradient. The collected FID is shown after an instrumental dead time. Without spatial resolution provided by the gradient, the spectra from the two spatially separated samples cannot be resolved. The spectra shown are a superposition of those from ^{14}N and ^{15}N, each showing auto-peaks and cross-peaks. (b) Contour plot of (a). Note that the horizontal arrows point to the ^{14}N peaks and the vertical arrows point to the ^{15}N peaks. Dashed arrows imply auto-peaks; the others are cross peaks.

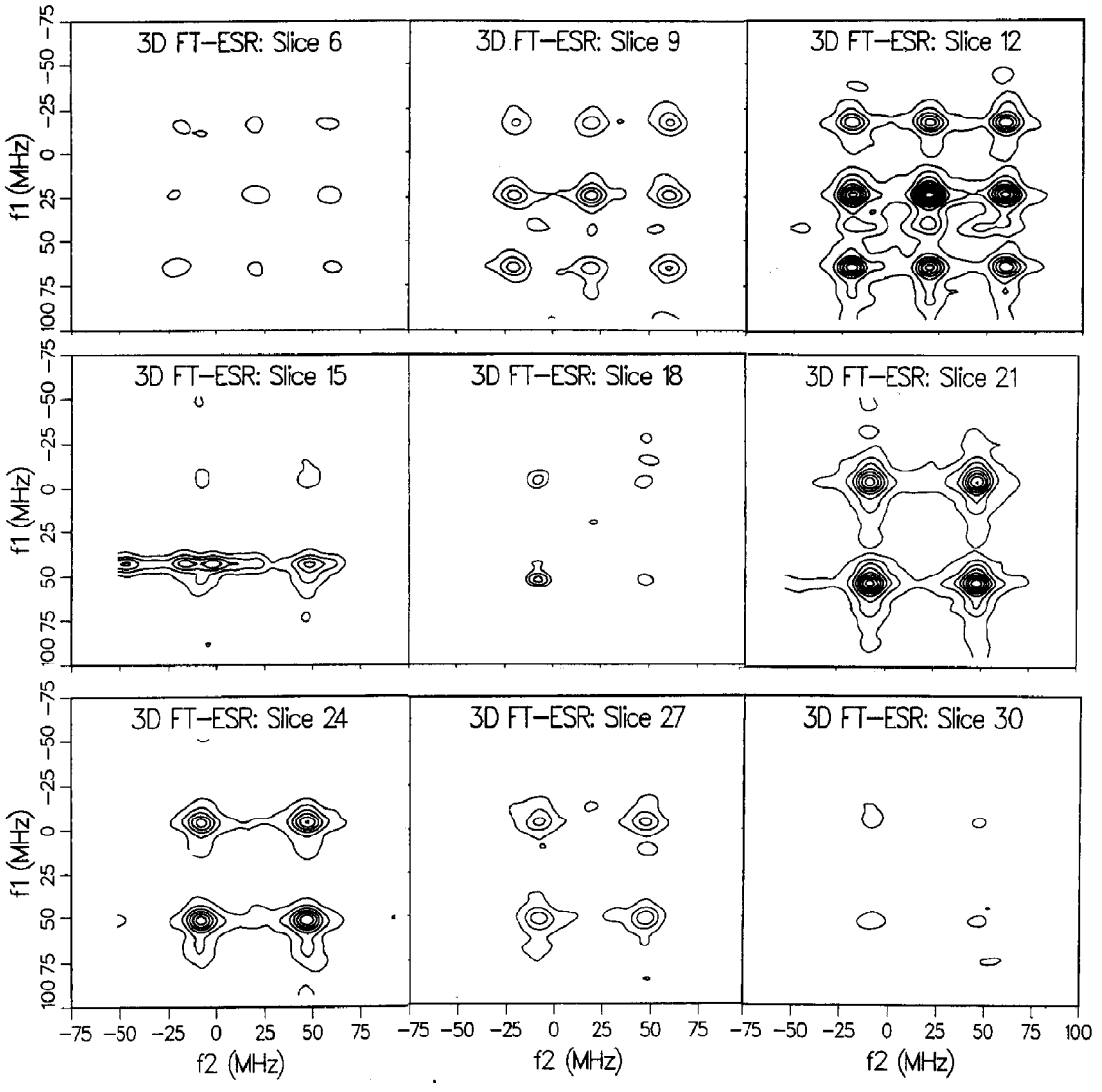

Fig. 2. With the application of a stepped gradient in the 2D-ELDOR experiment, we achieve good spatial resolution as shown in this series of contour plots each corresponding to a spatial slice perpendicular to the applied gradient.

3. Results

3.1. Spatially resolved 2D-ELDOR

The spatially resolved 2D-ELDOR experiment was performed as in fig. 3. The same sample as in ref. [1] (cf. fig. 1a of ref. [1]), consisting of two adjacent 1 mm inner diameter tubes containing either 4 mM ^{15}N tempone or 4.5 mM ^{14}N PDT in dodecane was utilized. We collected 2D-ELDOR spectra for each of 32 values of gradient G ranging from +80 to −80 G/cm. The spin evolution time, t_1 was ranged from 100 ns to 354 ns in 2 ns steps and the gradient was applied during the first 90 ns. (This yields a nominal resolution of 80 μm, cf. ref. [1].) The mixing time, T, was set at 300 ns. Each FID was collected as a function of t_2 in 1 ns steps starting from $t_{2,\,min} = 100$ ns extending to 355 ns. A 16 step phase cycle, which completely eliminates all transverse and axial peaks and at the same time eliminates all artifacts arising from incomplete quadrature orthogonality while canceling dc offsets, was utilized (cf.

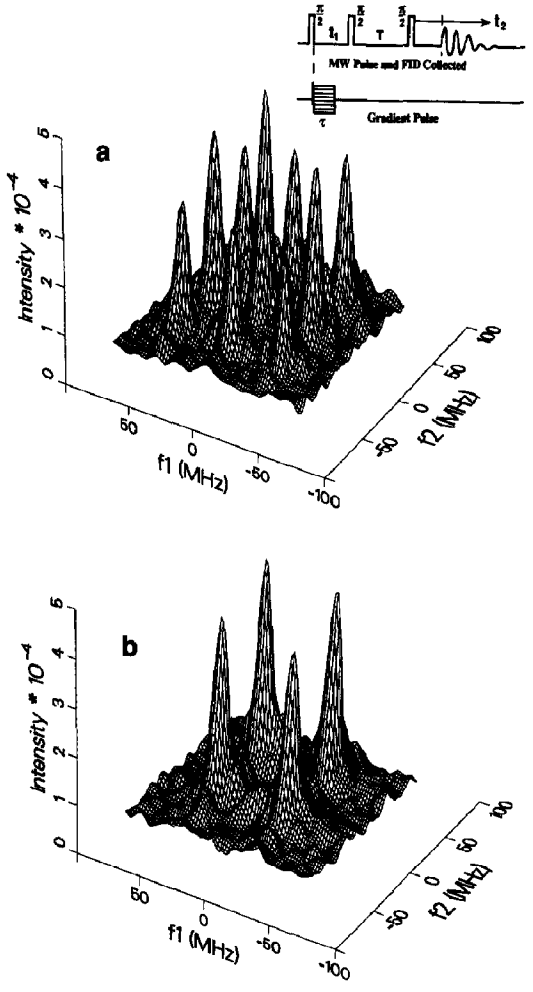

Fig. 3. Surface 2D-ELDOR plots of selected slices shown in fig. 2. (a) Slice 12 located near the center of the ^{14}N tube and (b) slice 21 from the ^{15}N tube. The pulse sequence for the phase encoded spatially resolved 2D-ELDOR experiment with gradient is shown as an insert.

table 4(b) in ref. [15]). Each step in the phase cycle was averaged 80 times. This phase cycle yields both S'_{ELDOR} and S''_{ELDOR}. We took the FFT with respect to t_2, and then the linear combination of dual quadrature signals given by $S_{c-} = S'_{ELDOR} - iS''_{ELDOR}$ [15]. (The S_{c+} combination [15], yields almost comparable spectra.) This was followed by an FFT with respect to $k = \gamma_e G\tau$ and then an FFT with respect to t_1. We display the magnitude spectra obtained from the complex S_{c-} signal.

In fig. 1 we show the 2D-ELDOR spectrum without the gradient pulse. All the peaks from the ^{15}N tempone and the ^{14}N PDT appear, including six cross-peaks due to HE between ^{14}N molecules, and two cross-peaks due to HE between ^{15}N molecules. Note the absence of ^{14}N–^{15}N cross-peaks, since the two types of nitroxide are non-interacting. (This spectrum corresponds to eq. (1) with $k=0$.) We next show in fig. 2 the spatially resolved 2D-ELDOR spectra as a series of contour plots (corresponding to the 2D-FT of eq. (2)). Each contour plot corresponds to a "slice" of the 3D spectral–spatial image that contains the 2D-ELDOR spectrum, at a given location along the Z axis. Slices 12 and 21 are located roughly at the centers of the two capillaries, and correspond to the 2D-ELDOR spectra of ^{14}N PDT and ^{15}N tempone respectively. (The spatial separation between adjacent slices is ca. 0.17 mm with the lowest numbered slices to the right of the tube of ^{14}N PDT and the highest numbered slices to the left of the tube of ^{15}N tempone.) One sees, that as we move from right to left the 2D-ELDOR spectrum of ^{14}N PDT shows up with a maximum at slice 12. It then fades out and the spectrum of ^{15}N tempone appears with a maximum at slice 21 and then fades out. The full 2D-ELDOR spectra of slices 12 and 21 are shown in fig. 3. A comparison of these spectra with fig. 1b clearly demonstrates that the 2D-ELDOR spectra of ^{14}N PDT and ^{15}N tempone have been spatially resolved.

3.2. Spin echoes

The sample we utilized for demonstrating FT-ESR imaging based upon spin-echoes was a hollow cylindrical quartz tube that had been γ-irradiated. The outer diameter was 3 mm. The effect of the application of a gradient of 66 G/cm is shown in fig. 4a to significantly shorten the echo decay into a window of 50 ns (which would be less than the minimum deadtimes currently achievable in a full power FID experiment) from a much longer echo decay corresponding to a $(T_2^*)^{-1} \approx 3$ G. We used a $\pi/2$–t_1–$\pi/2$–t_1–t_2 sequence in order to excite the same spectral range with each pulse. Data collection occurs during t_2. The FT of the right half of the echo decay, measured as a complex signal, yields the convolution of the spectrum with the spatial distribution. Previously, when a constant field gradient was utilized, a rather good 2D spatial–spatial image could be ob-

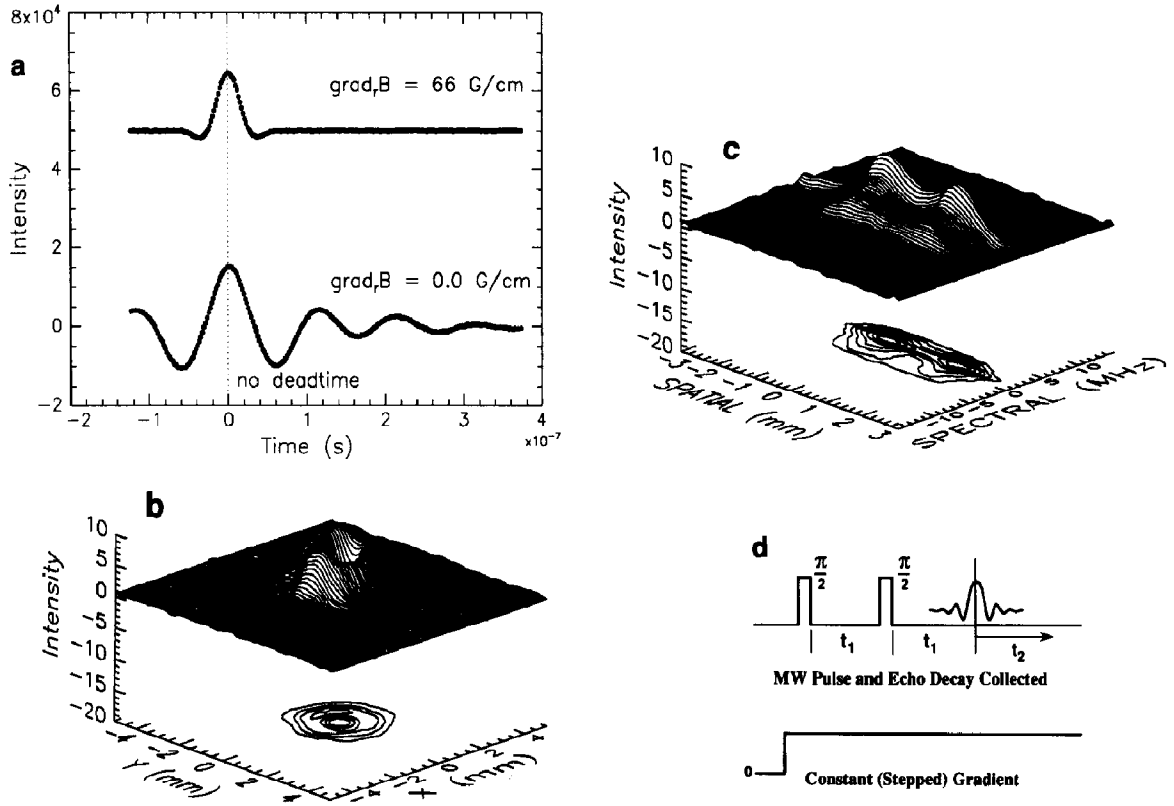

Fig. 4. Spin echo results. (a) Echo decay in the absence and presence of a constant gradient of 66 G/cm and a $B_1 = 15$ G. Note that although the T_2^* in the presence of the gradient is much reduced, the echo decay shape as a function of t_2 (equivalent to an FID decay in the present case where T_2 is uniform over the spectrum and there is no nuclear modulation) is easily measurable since there is no deadtime in t_2 in this experiment. (b) Sampling the echo decay shape as a function of sample rotation angle allows calculation of the spatial–spatial image shown here. (c) Collection of the echo decay shape as a function of gradient intensity permits calculation of the spectral–spatial image shown here as a surface plot of the spatially resolved ESR spectrum obtained in this experiment. (d) The pulse sequence for (c).

tained by rotating the sample in 5 degree steps and using projection reconstruction [16]. We show this 2D image in fig. 4b obtained with a gradient of 66 G/cm. The spectral–spatial image, fig. 4c, was obtained with multiple stepped constant gradients and collection of the echo decay shape, cf. fig. 4d. The constant gradient was varied over the range of ±190 G/cm. All projections with gradient values less than 30 G/cm utilized 10 averages per phase cycle step. For those with $G > 30$ G/cm, 100 collections were averaged to reduce differences in S/N. The 8-step phase-cycle given in Gamliel and Freed (cf. ref. [15], table 3b) was utilized, and the S_{c-} combination (cf. above) was used. The spectral–spatial distribution was calculated from the magnitude spectra (which is most conveniently obtained with our present software) of the measured echo decay (corresponding to eq. (6) with $k = \gamma_e G t_2$ and t_1 fixed at 400 ns) according to methods outlined elsewhere [17,18]. An advantage of utilizing echoes is that phase corrections due to finite deadtimes are eliminated but linear phase corrections are still, in general, required for off-resonance effects arising from finite microwave fields [19]. However, they are not important for the results in fig. 4. Use of magnitude spectra obviates the need for phase corrections.

In the spectral–spatial image of the γ-irradiated quartz tube, shown in fig. 4c, a spectral slice represents the typical inhomogeneously broadened spectrum for axial g-anisotropy and the spatial direction

shows the hollow cylinder geometry of the sample. The departure of this image from perfect cylindrical symmetry is probably due to the irradiated sample, since the experiment and analysis preserved cylindrical symmetry.

In conclusion, we note that modern FT-ESR imaging methods now allow for a wide range of rapid, spatially resolved one- and two-dimensional spectroscopies based upon either collection of FIDs or echo decays.

Acknowledgement

We thank Dr. David E. Budil for his 3D graphics efforts. This work was supported by NSF Grants DMR89-01718 and CHE90-04552 and NIH Grant GM-25862.

References

[1] U. Ewert, R.H. Crepeau, C.R. Dunnam, D. Xu, S. Lee and J.H. Freed, Chem. Phys. Letters 184 (1991) 25.
[2] J. Gorcester and J.H. Freed, J. Chem. Phys. 85 (1986) 5375.
[3] J. Gorcester, S. Rananavare and J.H. Freed, J. Chem. Phys. 90 (1989) 5764.
[4] J. Gorcester and J.H. Freed, J. Chem. Phys. 88 (1988) 4678.
[5] J. Gorcester, G.L. Millhauser and J.H. Freed, in: Advanced EPR: applications in biology and biochemistry, ed. A.J. Hoff (Elsevier, Amsterdam, 1989) ch. 5.
[6] J. Gorcester, G.L. Millhauser and J.H. Freed, in: Modern pulsed and continuous-wave electron spin resonance, eds. L. Kevan and M. Bowman (Wiley, New York, 1990) ch. 3.
[7] J. Gorcester and J.H. Freed, J. Magn. Reson. 78 (1988) 291.
[8] Y.-K. Shin, U. Ewert, D.E. Budil and J.H. Freed, Biophys. J. 59 (1991) 950.
[9] A. Nayeem, S. Rananavare, V.S.S. Sastry and J.H. Freed, J. Chem. Phys. 91 (1989) 6887.
[10] B.R. Patyal, R.H. Crepeau, D. Gamliel and J.H. Freed, Chem. Phys. Letters 175 (1990) 445.
[11] B.R. Patyal, R.H. Crepeau, D. Gamliel and J.H. Freed, Chem. Phys. Letters 175 (1990) 453.
[12] J.H. Freed, J. Chem. Soc. Faraday Trans. 86 (1990) 3173.
[13] A.D. Milov, A. Yu. Pusep, S.A. Dzuba and Yu. D. Tsvetkov, Chem. Phys. Letters 119 (1985) 421.
[14] D.J. Sloop, H.-L. Yu and T.S. Lin, Chem. Phys. Letters 124 (1986) 456.
[15] D. Gamliel and J.H. Freed, J. Magn. Reson. 89 (1990) 60.
[16] U. Ewert and J.H. Freed, 13th International EPR Symposium, Rocky Mountain Conference Denver, CO (1990).
[17] M.M. Maltempo, S.S. Eaton and G.R. Eaton, J. Magn. Reson. 77 (1988) 75.
[18] U. Ewert and T. Herrling, Chem. Phys. Letters 129 (1986) 516.
[19] J.P. Hornak and J.H. Freed, J. Magn. Reson. 67 (1986) 501.